Mesoporous Manganese Oxide Nanowires for High-Capacity, High-Rate, Hybrid Electrical Energy Storage

Wenbo Yan,[†] Talin Ayvazian,[†] Jungyun Kim,[†] Yu Liu,[‡] Keith C. Donavan,[†] Wendong Xing,[†] Yongan Yang,[†,¶] John C. Hemminger,[†] and Reginald M. Penner[†,§,*]

[†]Department of Chemistry, [‡]Department of Physics and Astronomy, and [§]Department of Chemical Engineering and Materials Science, University of California, Irvine, California 92697, United States. [¶]Present address: Department of Chemistry and Geochemistry, Colorado School of Mines, Golden, Colorado 80401.

Manganese oxide (MnO_2) is a material of long-standing interest for electrochemical energy storage, starting with its use in zinc−carbon Laclanché cells in the 1860s. Lee and Goodenough[1] discovered the application of MnO_2 to aqueous-based ultracapacitors in 1999. MnO_2 is composed of earth-abundant and nontoxic elements and its redox-active Mn centers can be charge-compensated by the intercalation of cations such as Li^+ and Na^+. The hybrid mechanism of charge storage operating in this material, involving double-layer charging as well as a change in Mn redox state, has been characterized in a large body of work (for reviews, see refs 2−5).

The driving force for investigating nanometer-scale MnO_2 materials is 2-fold: First, the wetted surface area of the material is increased as the critical dimension is reduced, leading to enhancement of the double-layer capacity, and second, the maximum distance over which charge compensating cations must diffuse is minimized, increasing the capacity at high charge−discharge rates.[3−5] With these motivations, MnO_x nanowires have been synthesized by many research groups who have also reported their electrochemical charge storage properties (Table 1). For example, Jiang et al.[6] prepared single crystalline, β-phase MnO_2 nanowires as small as ∼3−7 nm in diameter. These nanowires produced specific capacities, C_{sp}, of 279 F/g for constant current discharge at 1 A/g and 170 F/g for voltammetric cycling at 50 mV/s.[6] Somewhat higher C_{sp} values have been reported for template-synthesized nanotubes of polycrystalline MnO_2 (349 F/g[7] and 493 F/g[8]), whereas single crystalline MnO_2 nanotubes had a somewhat lower C_{sp} (220 F/g).[9] α-Phase MnO_2 nanorods with diameters of 20−50 nm produced a maximum C_{sp} of 233 F/g.[10]

ABSTRACT Arrays of mesoporous manganese dioxide, mp-MnO_2, nanowires were electrodeposited on glass and silicon surfaces using the lithographically patterned nanowire electrodeposition (LPNE) method. The electrodeposition procedure involved the application, in a $Mn(ClO_4)_2$-containing aqueous electrolyte, of a sequence of 0.60 V (*vs* MSE) voltage pulses delineated by 25 s rest intervals. This "multipulse" deposition program produced mp-MnO_2 nanowires with a total porosity of 43−56%. Transmission electron microscopy revealed the presence within these nanowires of a network of 3−5 nm diameter fibrils that were X-ray and electron amorphous, consistent with the measured porosity values. mp-MnO_2 nanowires were rectangular in cross-section with adjustable height, ranging from 21 to 63 nm, and adjustable width ranging from 200 to 600 nm. Arrays of 20 nm × 400 nm mp-MnO_2 nanowires were characterized by a specific capacitance, C_{sp}, of 923 ± 24 F/g at 5 mV/s and 484 ± 15 F/g at 100 mV/s. These C_{sp} values reflected true hybrid electrical energy storage with significant contributions from double-layer capacitance and noninsertion pseudocapacitance (38% for 20 nm × 400 nm nanowires at 5 mV/s) coupled with a Faradaic insertion capacity (62%). These two contributions to the total C_{sp} were deconvoluted as a function of the potential scan rate.

KEYWORDS: lithium ion · cathode · battery · electrodeposition · photolithography · electrodeposition · pseudocapacitance

In a separate category are multicomponent nanowires that contain one or more materials in addition to MnO_2 (Table 1). For example, Fan and co-workers[11] prepared MnO_2/CO_3O_4 core/shell nanowires with overall diameter in the 200 nm range using a three-step process. These hybrid nanowires yielded C_{sp} as high as 480 F/g for constant current discharge at ∼2.7 A/g.[11] Li and co-workers[12] coated MnO_2 onto carbon nanofibers and achieved C_{sp} as high as 365 F/g at 50 mV/s. Lee and co-workers[13] prepared composite nanowires of MnO_2 with the conductive polymer poly(3,4ethylenediosythiophene)-(PEDOT) that produced maximum C_{sp} of 250 F/g for discharge at 1.25 mA/cm². Composite nanowires of MnO_2 and silica produced C_{sp} of 151 F/g for high rate cycling at 100 mV/s.[14] The highest C_{sp} values reported for nanowires to our knowledge are those of Fan and Whittingham[15] who prepared poly-(methylmethacrylate)/Mn_3O_4 composite

TABLE 1. Performance of Some MnO$_2$ Supercapacitors/Cathodes

deposition method[a]	phase[b]	description[c]	electrolyte[d]	C_{sp}, F/g (scan/charge rate)	ref
			Nonaqueous		
RD	a	MnO$_2$/PEDOT np/nw	LiClO$_4$, PC	250 (1.25 mA/cm^2)	13
ES	s	PMMA/Mn$_3$O$_4$ nw	LiPF$_6$, EC/DMC	648–700 (0.5 mA/cm^2)	15
HT	s*	LiMn$_2$O$_4$ nw	LiClO$_4$, EC/DEC	354 (0.1 A/g)	40
ED	a	MnO$_2$/cnt	LiClO$_4$, PC	576 (10 mV/s)	41
ED	a	PANI/MnO$_2$ film	LiClO$_4$, AN	1292 (4 mA/cm^2)	42
RD	δ	MnO$_2$/cnt	LiClO$_4$, PC	250 (1 A/g)	43
			Aqueous		
HT	β	nw	Na$_2$SO$_4$	279 (1 A/g)	6
ED	a	nt	Na$_2$SO$_4$	349 (1 A/g)	7
ED	a	nw	Na$_2$SO$_4$	101 (10 mV/s)	7
ED	a	nw	Na$_2$SO$_4$	493 (4 A/g)	8
HT	α*	nt	Na$_2$SO$_4$	220 (5 mV/s)	9
PT	α	nr	Na$_2$SO$_4$	233 (5 mV/s)	10
RD	δ	MnO$_2$/C$_3$O$_4$ nw	LiOH	480 (2.7 A/g)	11
ED	α	MnO$_2$/cnf	Na$_2$SO$_4$	365 (50 mV/s)	12
PT	n/a	nw	Na$_2$SO$_4$/	151 (100 mV/s)	14
			+ 0–5% Silica		
ED	a	film	Na$_2$SO$_4$	1380 (5 mV/s)	16
ED	n/a	MnO$_x$ np/cnt	Na$_2$SO$_4$	1250 (1 A/g)	44
sol–gel	a	np	LiClO$_4$	720 (50 mV/s)	45
EP	n/a	ns/Au	Li$_2$SO$_4$	1145 (50 mV/s)	46
ED	n/a	film	Na$_2$SO$_4$	700 (0.16 mA/cm^2)	47
ED	a	MnO$_2$/cnt	LiClO$_4$	471 (10 mV/s)	41
ED	a	nw	LiClO$_4$	923 (5 mV/s)	this work
				484 (100 mV/s)	this work

[a] RD = redox deposition, ES = electrospinning, HT = hydrothermal, ED = electrodeposition, PT = precipitation, EP = electroless plating. [b] a = amorphous, s = spinel, *denotes single crystalline material. [c] nt = nanotube, nw = nanowire, np = nanoparticle, nr = nanorod, ns = nanosheet, cnt = carbon nanotube, cnf = carbon nanofiber, PEDOT = poly(ethylenedioxythiophene), PMMA = poly(methylmethacrylate), PANI = poly(aniline). [d] PC = propylene carbonate, PE = ethylene carbonate, AN = acetonitrile, DMC = dimethylcarbonate, DEC = diethyl carbonate.

nanowires by electrospinning. After annealing in air, these nanowires demonstrated a steady-state C_{sp} of 450–500 mAh/g for charge/discharge across 2.5 V corresponding to 648–700 F/g[15] but C_{sp} up to 1380 F/g has been reported for amorphous MnO$_2$ films[16] (Table 1).

In principle, significantly higher specific capacities should be accessible for MnO$_2$ nanowires. On the basis of Faraday's Law, the theoretical Faradaic capacity of the reaction:
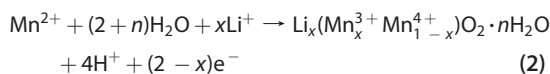
$$\text{Li}_x(\text{Mn}_x^{3+}\text{Mn}_{1-x}^{4+})\text{O}_2 + \delta\text{Li}^+ + \delta\text{e}^- \\ \rightarrow \text{Li}_{x+\delta}(\text{Mn}_{x+\delta}^{3+}\text{Mn}_{1-(x+\delta)}^{4+})\text{O}_2 \qquad (1)$$
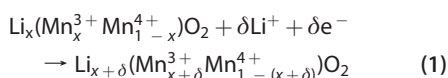
is 1110 C/g in the limit of $x = 0$,[17] corresponding to $C_{sp} = 1110$ F/g if this charge is delivered across a 1 volt window. This Faradaic capacitance should be augmented by a significant non-Faradaic capacity derived from double-layer charging of the MnO$_2$/electrolyte interface. But C_{sp} values greater than 1110 F/g have been reported in just a handful of cases (Table 1) and the fact that most experimental C_{sp} are far below this theoretical limit suggests that electrochemically inaccessible Mn$^{3+/4+}$ centers persist in nanometer-scaled MnO$_2$ even when the critical dimension of these materials is in the 10–20 nm range. The question arises, can higher C_{sp} be recovered from nanometer-scaled MnO$_2$ by shrinking the critical dimension below 10 nm?

To address this question, we have developed mesoporous MnO$_2$ (mp-MnO$_2$) nanowires that have a rectangular cross-section and minimum external dimensions of 20–53 nm in height and ~400 nm in width. These mp-MnO$_2$ nanowires are 43–56% porous with an internal morphology that is characterized by a network of amorphous MnO$_x$ fibrils 3–5 nm in diameter. mp-MnO$_2$ nanowires were prepared using a variant of the lithographically patterned nanowire electrodeposition (LPNE) method[18−20] in which MnO$_2$ is electrodeposited at a lithographically patterned gold electrode by applying a series of diffusion-controlled growth pulses in aqueous LiClO$_4$ electrolyte at a gold electrode confined within a lithographically defined template (Figure 1). We report the synthesis of mp-MnO$_2$ nanowires and the structural, chemical, and electrochemical characterization of these nanomaterials in this paper.

RESULTS AND DISCUSSION

Synthesis of mp-MnO$_2$ Nanowires Using LPNE. LPNE normally involves the preparation by photolithography of a patterned nickel electrode that is located within a horizontal trench.[18−20] Electrodeposition at this nickel electrode fills this trench, forming a nanowire of the electrodeposited material having a rectangular cross-section. This nickel electrode, and the photoresist that defines this horizontal trench, are both removed after the nanowire electrodeposition. Nickel works well in this process provided the nanowire can be formed using an electrochemical reduction (e.g., M^{n+} + ne$^-$ → M^0), but the nickel surface oxidizes rapidly during any anodization reaction in aqueous plating solutions, passivating it and rendering it useless for electrodeposition. Here, we obtain MnO$_2$ nanowires by the anodic reaction,

$$\text{Mn}^{2+} + (2+n)\text{H}_2\text{O} + x\text{Li}^+ \rightarrow \text{Li}_x(\text{Mn}_x^{3+}\text{Mn}_{1-x}^{4+})\text{O}_2 \cdot n\text{H}_2\text{O} \\ + 4\text{H}^+ + (2-x)\text{e}^- \qquad (2)$$

according to the procedure described by Popov and co-workers who reported $x = 0.35$ and $n \approx 1.0$.[21] In their experiments, δ-phase films of MnO$_2$ were obtained from dilute, aqueous Mn^{2+} solutions at room temperature by potentiostatic electrodeposition at +0.60 V versus saturated mercurous sulfate electrode (E$_{MSE}$ = +0.640 V vs the normal hydrogen electrode[22]).[21] We adapted the LPNE
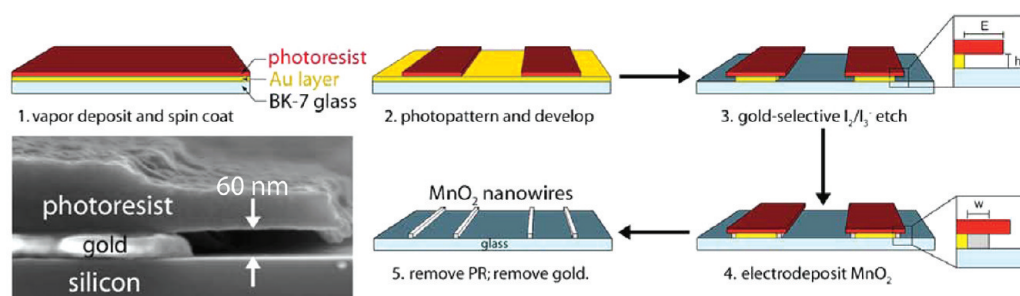
Figure 1. Schematic diagram depicting the process flow for the electrodeposition of MnO_2 nanowires using the lithographically patterned nanowire electrodeposition (LPNE) method. Inset (lower left): A scanning electron micrograph of a gold electrode and trench structure produced by the LPNE process.
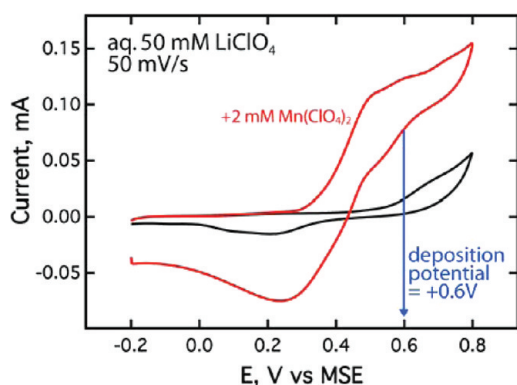

Figure 2. Cyclic voltammograms (50 mV/s) for a gold LPNE electrode (height = 40 nm) acquired in aqueous 50 mM $LiClO_4$ (black curve) and in the presence of added 2.0 mM $Mn(ClO_4)_2$ (red curve).

process to enable us to carry out reaction 1 by substituting a gold film for the nickel film (Figure 1). The etching of the gold electrode in step 3 and the subsequent removal of the gold electrode at the end of the LPNE process were both carried out using aqueous I_3^-/I_2. This gold electrode is shown in cross-section in the scanning electron microscopy (SEM) image shown in Figure 1 (left). Growth of the MnO_2 nanowire is confined to the trench defined on three sides by the gold electrode, the glass or silicon surface, and the photoresist layer. The height of this trench (~60 nm in Figure 1) can be controlled by varying the thickness of the gold layer, and the width of the trench (~200 nm in Figure 1) is adjusted by varying the duration of exposure to the I_3^-/I_2 etching solution.

A cyclic voltammogram acquired at an LPNE-patterned gold electrode (Figure 2) shows the onset of MnO_2 deposition at +0.30 V versus MSE. The quasi-limiting current behavior seen in this voltammogram, observed previously for the reductive deposition of metals at nickel LPNE electrodes,[18−20] is characteristic of a transport limited electrochemical process occurring at the recessed gold "nano-band" electrode that is embedded within the microfabricated template. The electrodeposition of MnO_2 nanowires was effected by applying +0.60 V versus MSE, a potential on this

limiting current plateau, in accordance with the prior work of Popov and co-workers.[21]

The electrodeposition of MnO_2 nanowires using the potentiostatic procedure[21] at +0.60 V (Figure 3a) causes rapid, diffusion-controlled MnO_2 growth (Figure 3b), and the resulting nanowires show evidence of the formation of dendritic asperities extending in the growth direction (Figure 3c). These "dendritic nanowires" are also discontinuous along their axes. To achieve growth at +0.60 V while simultaneously reducing the mean growth rate, we employed a multipulse strategy in which a train of 0.60 V pulses with a duration of 0.50 s were applied. These voltage pulses were separated from one another by 25 s rest periods each of which comprised a 20 s period at open circuit followed by 5 s at +0.30 V, a potential at which there is no significant MnO_2 growth. These rest periods are designed to permit the Mn^{2+}-depleted trench to diffusively refill with Mn^{2+} thereby eliminating dendritic MnO_2 growth, promoting a compact nanowire morphology (Figure 3f). The current versus time transients recorded during this growth process show an increasing current amplitude that is caused by reoxidation of the nascent and growing MnO_2 nanowire, coupled with the current associated with Mn^{2+} oxidation, following partial reduction of the nanowire during each +0.30 V rest period. We shall show that the MnO_2 nanowires prepared using this multipulse process are also mesoporous. Consequently, we refer to them as mp-MnO_2 nanowires.

An array of mp-MnO_2 nanowires deposited at 5 μm pitch is shown in the SEM image of Figure 4a. The height and width of these mp-MnO_2 nanowires can be independently varied without cross-talk. The nanowire height is controlled by the thickness of the gold film deposited in the first step of the LPNE process (Figure 1), whereas the nanowire width, from 200 to 600 nm, is proportional to the total electrodeposition time (Figure 4). A growth time of 7.5 s corresponds to the application of 15 × 0.5 s voltage pulses.

Characterization of MnO_2 Films and Nanowires. Grazing incidence X-ray diffraction (GIXRD) patterns were acquired for MnO_2 films electrodeposited on 40 nm-thick evaporated gold films on glass. In the case of MnO_2
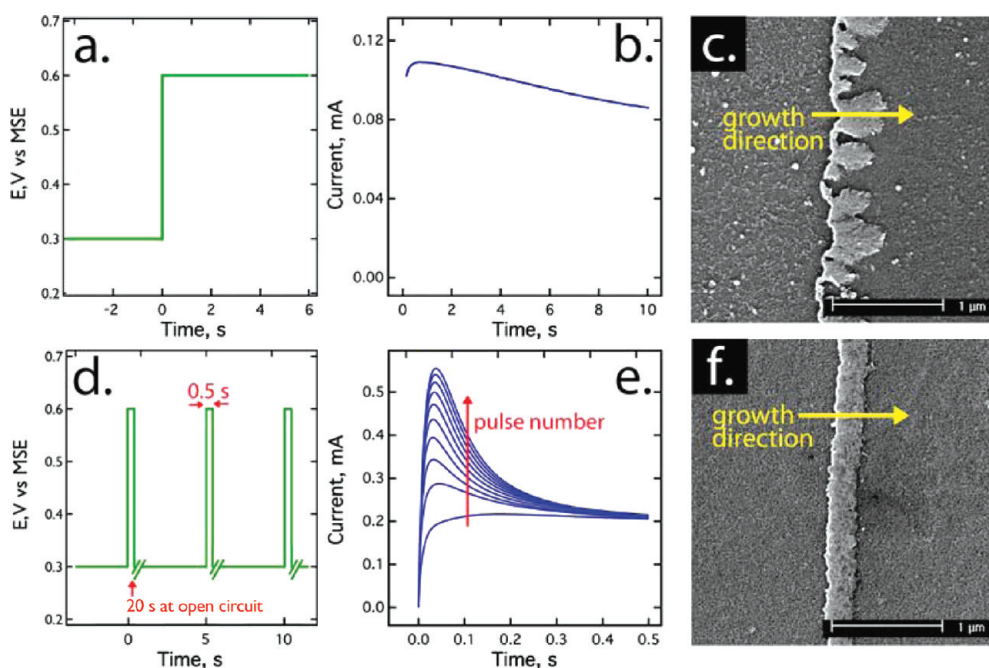
Figure 3. Multipulse synthesis of MnO₂ nanowires: (a) applied voltage program for the potentiostatic growth of MnO₂ nanowires; (b) current *versus* time for the potentiostatic growth of MnO₂ nanowires using the program shown in panel a in aqueous 2 mM Mn(ClO₄)₂, 50 mM LiClO₄; (c) SEM image of dendritic and discontinuous MnO₂ nanowire prepared potentiostatically; (d) multipulse program for potentiodynamic growth of MnO₂ nanowires; (e) current *versus* time transients showing the first 10 voltage pulses during potentiodynamic growth using the waveform shown in panel d; (f) compact MnO₂ nanowire morphology obtained using the multipulse deposition program.
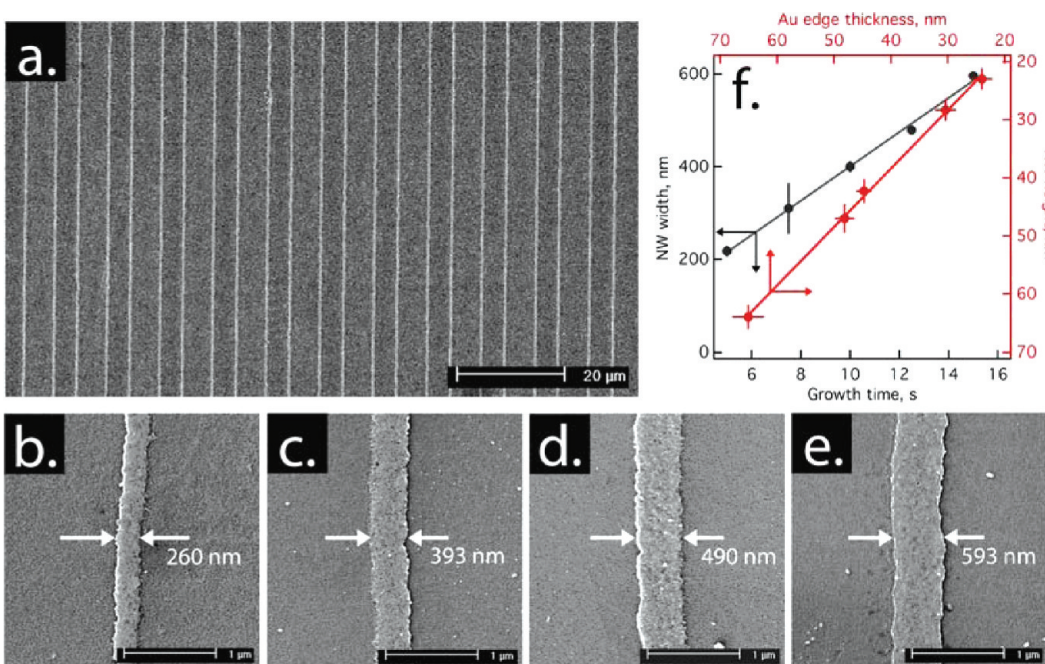
Figure 4. Control of nanowire width and height: (a) low magnification SEM image of an array of mp-MnO₂ nanowires; (b−e) mp-MnO₂ nanowires (height = 40 nm) prepared with a total deposition duration of 7.5 (b), 10.0 (c), 12.5 (d) and 15.0 s (e); (f) plots of nanowire height (red) and nanowire width (black), for nanowires with a height of 40 nm, as a function of gold edge thickness and growth time, respectively.

nanowires, arrays of linear nanowires were deposited at a 2 μm pitch on glass. MnO₂ films and dendritic nanowires (Figure 5a) both show reflections at 12.5° that can be indexed to (001) for δ-phase (birnessite)

MnO₂ (birnessite, JCPDS 43-1456). Scherrer analysis[23] of (001) line-width for films and dendritic nanowires yields a mean grain diameter of ∼5 nm. This reflection derives from the $d = 7.1$ Å periodicity of the O−Mn−O
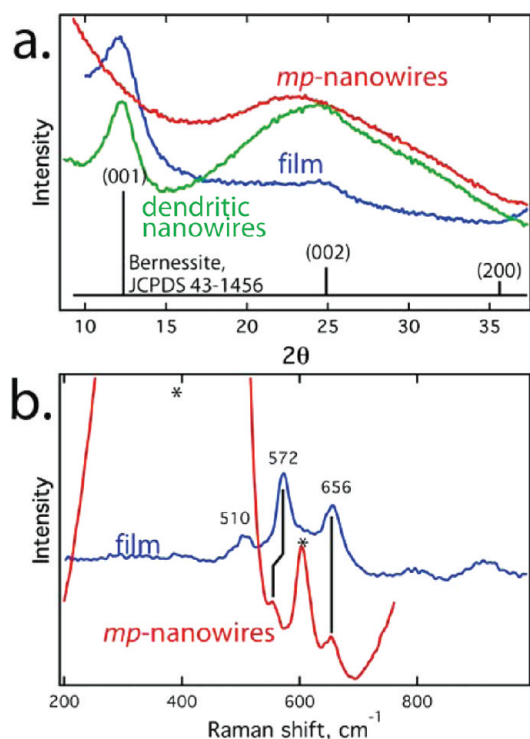
Figure 5. Grazing incidence X-ray diffraction (GIXRD) and Raman spectroscopy characterization of MnO$_2$ films and nanowires. (a) X-ray diffraction (XRD) patterns for a MnO$_2$ film prepared by multipulse deposition (blue), an array of mp-MnO$_2$ nanowires (red), and an array of dendritic MnO$_2$ nanowires prepared by potentiostatic deposition of MnO$_2$ at +0.60 V ("dendritic nanowires", green). (b) Raman spectra of a MnO$_2$ film prepared by multipulse deposition (blue, λ_{ex} = 532 nm) and a MnO$_2$ nanowire ("mp-nanowire") supported on quartz (red, λ_{ex} = 785 nm). Starred peaks are reflections from the quartz surface.

prismatic layers along the c-axis of the material. The broad reflection seen at ~23–25° is caused by diffuse scattering from the glass surface. mp-MnO$_2$ nanowires, on the other hand, were amorphous showing no reflections other than this diffuse scattering. Raman spectroscopy has proven to be a powerful, local structural probe for MnO$_2$.[24–27] δ-phase MnO$_2$ has strong Raman-active (Mn–O) stretching transitions at 646 and 575 cm^{-1}.[27] A somewhat weaker transition at 510 cm^{-1} is also prominent but less intense in most δ-phase MnO$_2$ samples.[27] All three of these characteristic Raman peaks are observed for MnO$_2$ films prepared using the multipulse procedure (Figure 5b), whereas a mp-MnO$_2$ nanowire prepared by multipulse deposition on quartz exhibits two of these—at 656 and 568 cm^{-1}. Peaks at lower energies, including the 510 cm^{-1} mode, cannot be observed because this spectral region is obscured by transitions of the quartz surface. Collectively the data of Figure 5 suggests that the mp-MnO$_2$ nanowires have some birnessite character despite being X-ray amorphous.

The surface chemical composition of MnO$_2$ films and mp-MnO$_2$ nanowires were examined using X-ray photoelectron spectroscopy (XPS). The Mn 2p spectra

region (Figure 6) showed a doublet of spin–orbit-coupled peaks consistent with the presence of a single chemical state for Mn. The binding energies (BEs) for the film and nanowires are similar, with nanowire BEs lower by about 0.50 eV (Figure 6). A literature survey (Table 2) reveals that nanowire Mn 2p BEs are in the range associated with MnO$_2$ and are significantly higher than BEs seen for plausible alternatives including M$_3$O$_4$, M$_2$O$_3$, and MnO.

To gain a better understanding of the MnO$_2$ produced by multipulse electrodeposition, we have also examined the Mn 3s and O 1s XPS spectral regions for MnO$_2$ films because an independent estimate of the Mn oxidation state in the film can be obtained from an analysis of these two spectra. The signal-to-noise in the Mn 3s spectral region for nanowire samples was too low to permit a detailed analysis because of the lower coverage of the surface by nanowires. In Figure 6 b,c, we compare three MnO$_2$ films that were freshly prepared ("as-prep"), and films that were transferred into Mn^{2+}-free aqueous 0.10 M LiClO$_4$ and then equilibrated at either +0.60 or −0.40 V. As-prepared MnO$_2$ films are effectively potentiostatted at +0.30 V because this is the "rest potential" at which the synthesis of these films is terminated during multipulse deposition (Figure 3d). For all three of these samples, the Mn 3s peak is split into two components, just as previously reported for MnO$_2$.[28,29] This splitting derives from an exchange interaction and its magnitude, ΔE, is linearly correlated with the mean valence, $\delta+$, of Mn in the MnO$_2$ sample over the range from δ = 2.0 (ΔE = 5.8 eV) to δ = 4.0 (4.0 eV).[28,29] We obtained ΔE = 4.9, 4.7, and 5.0 eV for the as-prepared, the −0.40 V, and +0.60 V films corresponding to δ = 3.7, 4.0, and 3.5, respectively (Table 3).[29] An independent estimate of $\delta+$ is obtained by analysis of the O 1s spectra region.[16,28,29] The oxygen 1s envelope can be fitted with three chemical shift components representing oxygen bonded to Mn$^{\delta+}$ with δ = 4.0 corresponding to an Mn–O–Mn species (529.8 ± 0.1 eV), a second component representing oxygen bonding to δ = 3.0 Mn corresponding to a Mn–OH species (531.1 ± 0.2 eV) and, finally, oxygens present in residual water (H–O–H) are represented by the third 532.5 ± 0.1 eV component. The value of δ is obtained using[16]

$$\delta = \frac{[(+4)S_{Mn-O-Mn} - S_{Mn-OH}] + [(+3)S_{Mn-OH}]}{S_{Mn-O-Mn}}$$

(3)

where $S_{Mn-O-Mn}$ and S_{Mn-OH} are the fractional photoelectron intensities attributable to these two chemical shift components. From this analysis, we obtain δ = 3.49, 3.71, and 3.93 for the −0.40 V, as-prepared, and +0.60 V films, respectively. These values are close to those we obtain from the Mn 3s ΔE measurement (Table 3). The value of δ for as-prepared multipulse MnO$_2$ of 3.70 corresponds to a value of x = 0.30 in eq 1,
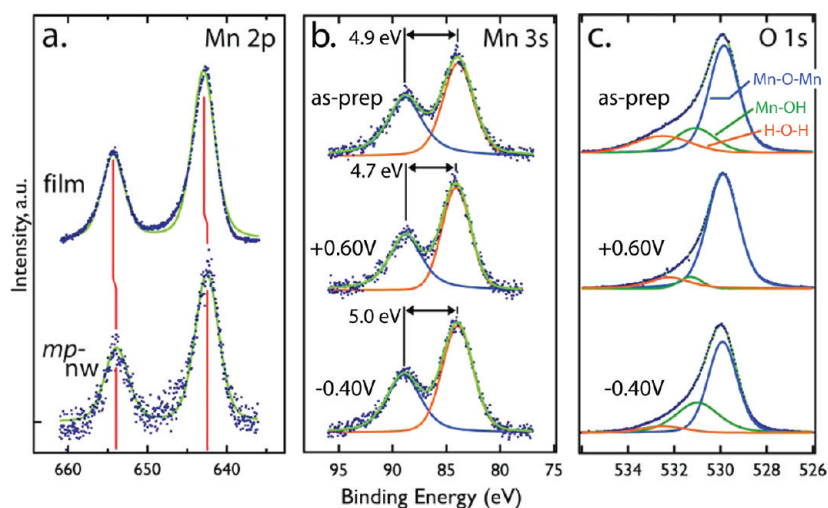
Figure 6. X-ray photoelectron spectra (XPS) for MnO_2 films prepared by multipulse deposition and mp-MnO_2 nanowires: (a) Mn 2p spectral region for a film and an array of mp-MnO_2 nanowires; (b) Mn 3s spectral region for MnO_2 films. As-prepared films were effectively equilibrated at +0.30 V during synthesis since this is the "rest potential" between +0.60 V synthesis pulses. (c) O 1s spectra region for the same films shown in panel b. O 1s photoelectron spectra are shown with a deconvolution into three chemical states as previously described by Bélanger and co-workers.[16]

TABLE 2. Comparison of Measured Mn 2p Binding Energies for mp-MnO_2 Nanowires and MnO_2 Films with Literature Values for Various Compounds

	binding energy (eV)		
sample	Mn 2p$_{1/2}$	Mn 2p$_{3/2}$	ref
MnO	653.4	640.4—641.7	48—55
Mn_2O_3	653.4—653.7	641.2—642.0	48—52,54—56
Mn_3O_4	653.1—653.2	641.1—641.9	48—51,54—56
MnO_2	653.8—653.9	642.0—642.8	39,48,51—58
film	654.3	642.9	this work
nanowire	653.9	642.5	this work

TABLE 3. XPS Data for As-Prepared, Oxidized (+0.60 V), and Reduced (−0.40 V) MnO_2 Films

	Mn 3s			O 1s			ox. state
sample	BE$_1$ (eV)[c]	BE$_2$ (eV)[c]	ΔE[d]	state[e]	BE (eV)[e]	area %	Mn 3s/O 1s[f]
as-prepared[a]	88.84	83.94	4.90	Mn—O—Mn	529.85	64	3.70/3.71
				Mn—O—H	531.10	19	
				H—O—H	532.50	17	
+0.6 V[b]	88.76	84.06	4.70	Mn—O—Mn	529.90	83	4.00/3.93
				Mn—O—H	531.3	6	
				H—O—H	532.26	11	
−0.40 V[b]	88.95	83.95	5.00	Mn—O—Mn	529.91	62	3.50/3.49
				Mn—O—H	531.00	32	
				H—O—H	532.50	6	

[a] As-prepared MnO_2 films were removed from the deposition solution immediately after deposition, rinsed with Millipore water, and air-dried prior to XPS analysis. [b] MnO_2 films prepared at +0.60 or −0.40 V were transferred from the deposition solution into aqueous, 0.10 M $LiClO_4$ and potentiostatted at either potential for 10 min. [c] Two chemical states, with discrete binding energies as indicated, were observed for Mn 3s photoelectrons. [d] $\Delta E = BE_1 - BE_2$. [e] Three chemical states with discrete binding energies as indicated, were observed for O 1s photoelectrons [f] The oxidation state of the MnO_2 film was calculated two ways: 1) Analysis of the Mn 3s peak splitting (column ΔE above) in conjunction with the calibration of this shift in terms of the oxidation state from prior work,[28,29] and 2) Analysis of the O 1s spectral region, with deconvolution of three chemical shift components tabulated here, in conjunction with eq 3 as described in the text.

close to the value $x = 0.35$ reported by Popov and co-workers.[21] An independent estimate of x is obtained from an analysis of the deposited MnO_2 mass, and we discuss this measurement next.

The specific capacitance, C_{sp}, of MnO_2 films and nanowires was calculated from cyclic voltammograms acquired in aqueous 0.10 M $LiClO_4$ using

$$C_{sp} = \frac{Q}{\Delta E \times m} \tag{4}$$

where Q is the total charge associated with scanning from −0.40 to +0.60 V, ΔE is 1.0 V, and m is the dry mass of the MnO_2. If, instead, Q was measured using a negative-going scan from +0.60 to −0.40 V, identical values were obtained to within ±2%. To obtain m from the deposition charge with high precision, we directly measured the value of x in eq 1. The deposited MnO_2 mass was measured using a quartz crystal microbalance (QCM) first *in situ*, during the deposition process, and then after drying in vacuum for 2 h at room temperature (Figure 7a). This drying protocol removes only superficial water adsorbed on the outside of MnO_2
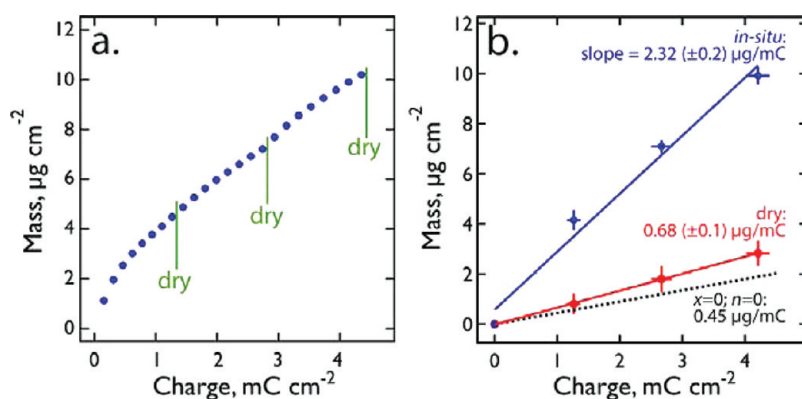
crystallites, not intercalated water which is desorbed at 100 °C and above.[30] We interrupted the multipulse deposition of MnO_2 after 8, 16, and 24 pulses to vacuum-dry the film and measure the mass of the dried film (Figure 7a). Mass *versus* charge plots were approximately linear (Figure 7a) and the slope of the

Figure 7. Determination of x eq 1 for MnO_2 multipulse electrodeposition. (a) Example of a typical mass *versus* deposition charge measurement for the multipulse electrodeposition of a MnO_2 film on gold. Each data point represents the charge associated with a single growth pulse. The deposition was stopped after the application of 8 pulses, 16 pulses, and 24 pulses (as indicated). At each of these three points, the QCM crystal was removed from the plating solution, rinsed in water, dried for 2 h in vacuum, and the dry mass of the film was measured. This film was then reimmersed in the plating solution, and the deposition was resumed. (b) Mean mass *versus* mean charge for five replicate depositions showing the slope obtained for the *in situ* mass measurement (blue) and that of the vacuum-dried film (red). Assuming all of the mass change derives from the removal of superficial water and that $n = 1$, this slope corresponds to $x = 0.36$ eq 2. The wet state of the film has ∼14 superficial water molecules per Mn in this case. Also shown (dashed line) is the predicted slope for the case of $x = 0$ and $n = 0$ in eq 2.

data was not altered by interrupting the deposition to dry the film. Mean mass *versus* mean charge data for five replicate samples (Figure 7b) produced slopes of 2.32 ($\pm$0.2) μg/mC for the *in situ* measurement and 0.68 ($\pm$0.1) μg/mC for the dried film. This latter value was used to determine film and nanowire masses from the deposition charge as required for the calculation of C_{sp} in eq 4.

The number of superficial waters present in the as-deposited film and the value of x in eq 2 are both obtained from the data of Figure 7. If it is assumed that $n = 1.0$ in eq 2,[21,31] approximately 14.3 superficial water molecules are codeposited with each Mn and $x = 0.36$. The porosity of the MnO_2 films and nanowires may also be obtained if the volume of these structures is known:

$$\text{porosity} = 1 - \frac{\rho_{expt}}{\rho_{theor}} \qquad (5)$$

where ρ_{expt} is the measured density and ρ_{theor} is the density of the nonporous birnessite (3.4 g/cm^3).[32] ρ_{expt} was obtained from m and the height and width of MnO_2 nanowires measured by atomic force microscopy (AFM). Porosities were also obtained for MnO_2 films where the film thickness was measured by AFM. The porosity of mp-MnO_2 nanowires was in the range from 43% to 56%, whereas that of MnO_2 films was 83% to 92% (Table 4).

Transmission electron microscopy (TEM) was carried out on arrays of nanowires with a thickness of 20 nm that were deposited at 5 μm pitch on a Si grid with 20 nm thick Si_3N_4 "windows". Within these nanowires (Figure 8) are a two-dimensional "net" of 3−5 nm electron dense fibrils, accounting at least qualitatively for the 43−56% porosity deduced from the QCM and AFM measurements. These fibrils did not have discernible atomic resolution structure and no crystallinity was revealed by selected area electron diffraction analysis.

TABLE 4. Calculation of Nanowire and Film Porosities from AFM and QCM Data

sample	mass^a (μg)	ρ_{expt}^{b} (g/cm^3)	porosity^c
mp-MnO_2 Nanowires			
20 × 400 ($\pm$13) nm nw	1.23 ($\pm$0.05)	1.92	43 ($\pm$2)%
35 × 400 ($\pm$13) nm nw	1.66 ($\pm$0.27)	1.48	56 ($\pm$9)%
50 × 400 ($\pm$13) nm nw	2.39 ($\pm$0.00)	1.49	56 ($\pm$2)%
MnO_2 Films^d			
60 nm film	4.11	0.500	85%
80 nm film	6.52	0.595	83%
280 nm film	10.23	0.267	92%

^{a} Measured by QCM on four vacuum-dried mp-MnO_2 nanowire samples. ^{b} Mass from column 2 divided by the AFM-measured volume. ^{c} Calculated using eq 4 assuming the density of nonporous birnessite, ρ_{theor}, is 3.40 g/cm^3.[32] ^{d} The film area was 137 cm^2.

We examined the voltammetry of arrays of mp-MnO_2 nanowires within the LPNE template in which they were deposited. This practice ensured intimate electrical contact to the nanowire by the same gold electrode on which it was electrodeposited; however, just one edge of the nanowire is wetted by the electrolyte in this case (Figure 9a, inset). In other words, within this microfabricated trench, access of the electrolyte to the surfaces of the MnO_2 nanowire are blocked on three sides: on the top of the nanowire by the photoresist, on one edge of the nanowire by the gold electrode, and on the bottom of the nanowire by the glass surface leaving just one edge of the nanowire exposed to solution. The capacitive current measured for the gold LPNE template is increased by a factor of 5 upon deposition of the mp-MnO_2 nanowire (Figure 9a). In principle, three processes contribute to the currents measured for the mp-MnO_2 nanowire: (1) double-layer charging of MnO_2 surfaces, (2) pseudocapacitive

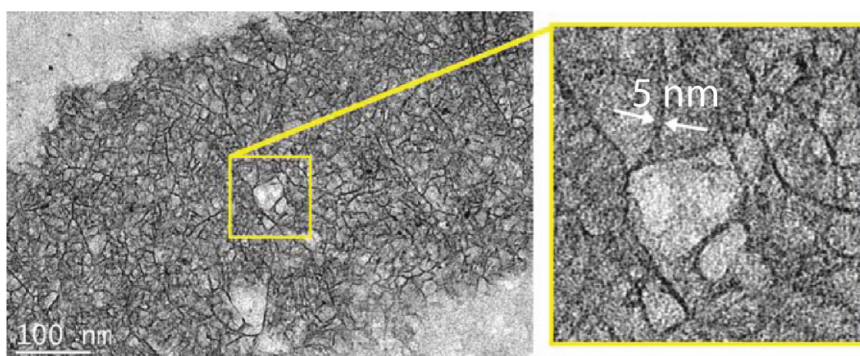**Figure 8.** Transmission electron micrograph (TEM) of a 20 nm (*h*) × 400 nm (*w*) mp-MnO$_2$ nanowire showing porosity and the organization of the MnO$_2$ into 3−5 nm fibrils.
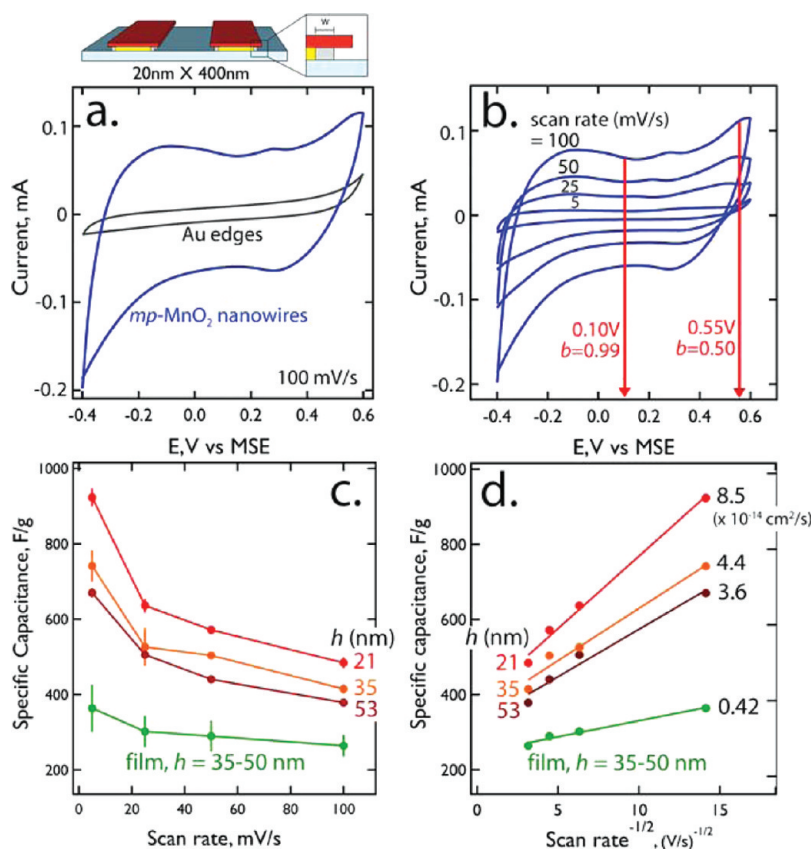

Figure 9. Cyclic voltammetry (CV) of MnO$_2$ nanowires and films in aqueous 0.10 M LiClO$_4$. (a) CVs (100 mV/s) for an LPNE-templated gold electrode (Figure 9a, inset) before (black) and after (blue) deposition of a 20 nm × 400 nm mp-MnO$_2$ nanowire. (b) Scan rate dependence for the CV of a 20 nm × 400 nm mp-MnO$_2$ nanowire. The *b* parameter was calculated at two potentials from these data: +0.10 V (*b* = 0.99) and +0.55 V (*b* = 0.50). (c) C_{sp} *versus* scan rate for three mp-MnO$_2$ nanowires with thicknesses of 21, 35, and 53 nm as indicated, as well as three MnO$_2$ films with thickness in the range from 35 to 50 nm (average C_{sp} data are shown). (d) C_{sp} *versus* (scan rate)$^{-1/2}$ for the same data shown in panel c. Diffusion coefficient values were obtained from the slopes of these plots using eq 6.

Faradaic current associated with redox reactions of surface Mn$^{3+/4+}$ centers, and, (3) Faradaic reactions of Mn$^{3+/4+}$ centers requiring Li$^+$ insertion/deinsertion for charge compensation. The scan rate (ν)-dependent current (*i*, Figure 9b) is described by the generic reaction:[33,34] $i = a\nu^b$, where *a* is a constant that depends upon the electrode area, the concentration of Mn$^{3+/4+}$ redox centers, and the diffusion coefficient for charge

transport in the MnO$_2$.[22] Two limiting values exist for *b*: *b* = 0.5 for a voltammetric process that is controlled by linear diffusion to a planar electrode surface (*e.g.*, process 3) while *b* = 1.0 for surface-limited processes including double-layer charging and pseudocapacitive charge transfer at surface Mn$^{3+/4+}$ centers (processes 1 and 2).[22] We observe both of these limits in the data of Figure 9b: At *E* = 0.10 V, *b* = 0.99 indicating that
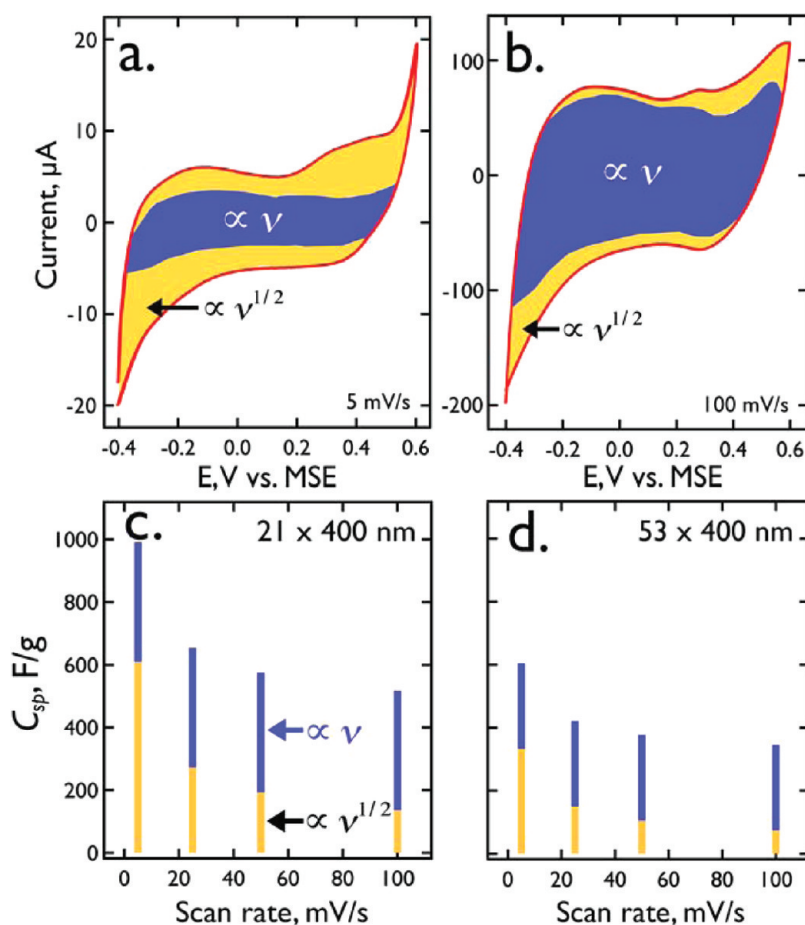
Figure 10. Deconvolution of two capacity components: Faradaic insertion capacity ($\propto \nu^{1/2}$, yellow) and double-layer charging and Faradaic pseudocapacity ($\propto \nu$, blue). (a,b) CVs at 5 mV/s (a) and 100 mV/s (b) for an array of 21 nm $\times$ 400 nm mp-MnO$_2$ nanowires showing the two capacity components after deconvolution using eq 8, (c,d) Bar graphs of the two C_{sp} components versus ν for mp-MnO$_2$ of two different heights: 21 (c) and 53 nm (d).

processes 1 and 2 dominate the current. At $E = 0.55$ V, $b = 0.50$ indicating the process 3 dominates the current. But we can perform a deconvolution of processes 1, 2, and process 3 at each potential across this 1.0 V scan range using the procedure described below.

The C_{sp} for arrays of mp-MnO$_2$ nanowires and MnO$_2$ films was calculated using data like that shown in Figure 9b using eq 4. Plots of C_{sp} versus potential scan rate, ν (Figure 9c) show increasing C_{sp} with decreasing ν, just as observed in many previous studies. This behavior has been attributed to rate-limiting Li$^+$ insertion and solid-state diffusion. C_{sp} also increases as the nanowire height is reduced from 53 to 21 nm while all three nanowire heights produced C_{sp} values that were significantly higher than those measured for MnO$_2$ films. The maximum C_{sp} value seen for $h = 21$ nm mp-MnO$_2$ nanowires was 923 ± 24 F/g at $\nu = 5$ mV/s. This value can be compared with the theoretical C_{sp} based upon eq 1 with $x = 0.36$, which is 690 F/g. The fact that the experimental C_{sp} exceeds this value by 30% suggests that the Faradaic capacity of the material is augmented by a significant double-layer capacity component.

If it can be assumed that the C_{sp} value observed at each scan rate is limited by diffusion of Li$^+$, then C_{sp} should be proportional to $\nu^{1/2}$ and this proportionality is observed for our data (Figure 9d). The diffusion coefficient for Li$^+$, D_{Li+}, can then be estimated from the slope of this plot using

$$Q(\nu) = \frac{2nFAD_{Li^+}^{1/2}C^*}{\pi^{1/2}}\left(\frac{RT}{F\nu}\right)^{1/2} \tag{6}$$

Here, $Q(\nu) = C_{sp}$ for the case where the scan range over which $Q(\nu)$ is integrated equals 1.0 V. Equation 6 is obtained from the integrated Cottrell equation[22] by substituting the quantity ($RT/F\nu$) for t where R is the gas constant, F is the Faraday constant, C^* is the concentration of Mn redox centers calculated from the density (Table 4), and A is the wetted area of the MnO$_2$ nanowire or film. The D_{Li^+} values obtained from eq 6 are in the 10^{-13} to 10^{-14} cm^2/s range (Figure 9d), but it is highly unlikely that these values have physical relevance since the actual wetted surface area of the MnO$_2$ nanofibril network within the nanowire is orders of magnitude higher than the geometric area of the wetted nanowire within the LPNE template used to

calculate these D_{Li+} values. Although eq 6 describes planar not cylindrical diffusion, it is apparent that the enormous internal surface area of the mp-MnO$_2$ nanowires requires a D_{Li+} that is orders of magnitude lower than the values calculated in Figure 9d. Unfortunately, the precise wetted surface interior surface area of these films is not easily estimated or measured.

Conway[35] and Dunn[36,37] have demonstrated an elegant method for deconvoluting the C_{sp} into two components corresponding to the two values of b already mentioned above: $b = 1.0$ corresponding to the case $i(v) \propto v$, encompassing double-layer charging and the pseudocapacitance of Mn centers located at MnO$_2$ surfaces, and $b = 0.5$ corresponding to the case $i(v) \propto v^{1/2}$ which is the current component derived from diffusion-limited cation intercalation/deintercalation. For a scan rate series (e.g., Figure 9b), the total current measured at each potential, $i(v)$, is given by the sum of these two components:[33,35,37]

$$i(v) = k_1 v + k_2 v^{1/2} \qquad (7)$$

where k_1 and k_2 are scan rate independent constants. By plotting the quotient $(i(v)/v^{1/2})$ versus $v^{1/2}$, the values of k_1 and k_2 are obtained from the slope and intercept, respectively.

$$\frac{i(v)}{v^{1/2}} = k_1 v^{1/2} + k_2 \qquad (8)$$

The outcome of a deconvolution of $i(v) \propto v$ and $i(v) \propto v^{1/2}$ capacity components for 21 × 400 nm mp-MnO$_2$ nanowires (Figure 10a,b) reveals that Faradaic insertion capacity is concentrated at the positive and negative extremes of the 1.0 V scan range while non-Faradaic and pseudocapacitive contributions are distributed approximately uniformly across this potential range. Since we can show, using chronocoulometry for example, that redox species in solution do not contribute significantly to the currents we measure, we conclude that all of the Faradaic current detected here derives from the interconversion of Mn^{3+}/Mn^{4+} in the mp-MnO$_2$ nanowires.

The scan rate dependence of this deconvolution is of particular interest (Figure 10c,d). Here we see that the non-Faradaic and pseudocapacitive contribution to C_{sp} (i.e., $i(v) \propto v$) is virtually scan-rate independent while that of the Faradaic insertion contribution to C_{sp} (i.e., $i(v) \propto v^{1/2}$) decreases with increasing scan rate. At 100 mV/s, C_{sp} is dominated by noninsertion processes (75% of C_{sp}) while at 5 mV/s the insertion capacity is dominant (60% of C_{sp}). The maximum Faradaic insertion capacity we obtain (∼600 F/g) remains somewhat lower than predicted by eq 1 with $x = 0.36$ (690 F/g).

CONCLUSIONS

The main conclusions of this work are the following:

1. mp-MnO$_2$ nanowires can be electrodeposited using a pulsed electrodeposition program within a lithographically patterned gold template. Our method provides control over the external dimensions of these nanowires including the nanowire width and height, down to minimum values of 20 nm (height) and 200 nm (width).

2. These mp-MnO$_2$ nanowires are amorphous to X-rays and electrons, but Raman transitions consistent with δ-phase MnO$_2$ are observed for these nanowires. XPS and QCM independently estimate x eqs 1 and 2 in (Mn$_x^{3+}$ Mn$_{1-x}^{4+}$)O$_2$ as 0.30 and 0.36, respectively.

3. C_{sp} values measured by cyclic voltammetry are correlated with the nanowire height; the largest C_{sp} values measured in this study were 923 F/g at 5 mV/s and 484 ± 15 F/g at 100 mV/s. The latter value is among the largest seen at this high scan rate for MnO$_2$ in any previous study. The 923 F/g value exceeds by 34% the expected Faradaic capacity of these nanowires based upon our measured value of x.

4. Using the method of Conway[35] and Dunn,[36,37] Faradaic insertion and noninsertion contributions to the total C_{sp} can be cleanly deconvoluted revealing that mp-MnO$_2$ nanowires behave like supercapacitors at high scan rates (100 mV/s)) while exhibiting true hybrid energy storage at low scan rates (5 mV/s).

5. The ultrahigh internal surface area of mp-MnO$_2$ nanowires translates into C_{sp} values at 100 mV/s of up to 484 F/g; among the highest reported to date.

EXPERIMENTAL SECTION

Chemicals and Materials. Manganese perchlorate hydrate (Mn(ClO$_4$)$_2$· H$_2$O, 99%), lithium perchlorate (LiClO$_4$, 95%), silver sulfate (Ag$_2$SO$_4$, 5 N), and iodine (I$_2$, 99.8%) were used as received from Sigma-Aldrich. Sulfuric acid (ULTREX ultrapure) was purchased from J. T. Baker. Potassium iodide (KI, 99%), acetone, methanol, and nitric acid were used as received from Fisher (ACS Certified). Positive photoresists, Shipley S-1808 and S-1827 and developer MF-319 were purchased from Microchem Corporation. Gold pellets (5 N purity, ESPI Metals) were used for the evaporation of films.

MnO$_2$ Nanowire Synthesis. MnO$_2$ nanowire arrays were prepared by electrodeposition using the LPNE process.[18−20] Gold films 20−70 nm in thickness were thermally evaporated onto precleaned 1″ × 1″ squares of soda lime glass. A positive photoresist (PR) layer (Shipley, S1808) was deposited by spin-coating (2500 rpm, 80 s) resulting in a PR layer of ∼800 nm thickness after soft-baking (90 °C, 30 min). This PR was then patterned using a contact mask in conjunction with a UV light source equipped with a shutter and photolithographic alignment fixture (Newport, 83210i-line, 365 nm, 1.80 s). The exposed PR region was developed for 15 s (Shipley, MF-319), rinsed with

Millipore water (Milli-Q, $\rho > 18$ M$\Omega \cdot$cm), and air-dried. Exposed gold was removed by dipping the patterned samples in KI/I$_2$/H$_2$O (4/2/40 g) (Fisher, ACS Certified) solution for 8 s (for a 40 nm gold layer thickness) to create a horizontal trench with a typical width of 500 nm and a height that equaled the thickness of the evaporated gold layer. The entire lithographically patterned region was then immersed in an aqueous plating solution with the exception of one edge where an electrical contact to the gold layer was established using an alligator clip. MnO$_2$ deposition was effected by either stepping the potential to +0.60 V versus Hg/Hg$_2$SO$_4$, K$_2$SO$_4$ (saturated) (MSE) or by pulsing the potential to this potential, as described in the text. Electrodeposition was conducted using a one-compartment three-electrode electrochemical cell using a Princeton Applied Research 2263 potentiostat. After the MnO$_2$ electrodeposition was complete, the remaining PR was removed by rinsing with acetone (Fisher, ACS Certified) and Milli-Q water, and the remaining gold was removed by soaking in a KI/I$_2$ solution for 1 min. This process produced an array of MnO$_2$ nanowires that strongly adhered to the surface of the glass substrate.

Electrochemical Characterization. All electrochemical measurements were conducted using a one-compartment three-electrode electrochemical cell using a Princeton Applied Research 2263 potentiostat. The aqueous solutions used in these analyses were not degassed because the removal of O$_2$ had no detectible influence of the observed voltammetry or on the values of the specific capacitances that we measured. A platinum flag counter electrode was used in conjunction with a saturated mercurous sulfate reference electrode (MSE) for these measurements. All potentials are quoted with respect to this reference (E_{MSE} = +0.640 V vs normal hydrogen electrode).

Structural Characterization. Scanning electron micrographs were acquired by using a Philips XL-30 FEG SEM (field emission gun scanning electron microscope) operated at 10 keV. All samples were sputtered with a thin layer of Au/Pd before imaging to prevent charging.

Transmission electron microscopy (TEM) images and selective area electron diffraction (SAED) patterns were obtained using a Philips CM 20 TEM operating at 200 keV. The MnO$_2$ nanowires were potentiodynamically synthesized onto a Si grid with 20 nm thick Si$_3$N$_4$ windows (Ted Pella, Inc.).

Atomic force microscopy (AFM) images and amplitude traces were acquired using an Asylum Research, MFP-3D AFM equipped with Olympus, AC160TS tips in a laboratory air ambient.

Grazing-incidence X-ray diffraction (GIXRD) patterns were obtained using a Rigaku Ultima III high resolution X-ray diffractometer employing the parallel beam optics with a fixed incident angle of 0.3°. The X-ray generator was operated at 40 kV and 44 mA with Cu Kα irradiation. The JADE 7.0 (Materials Data, Inc.) X-ray pattern data processing software was used to analyze acquired patterns and estimate the respective grain diameter size.

Raman Spectroscopy. Raman spectra were collected using a Renishaw inVia Raman Microscope equipped with the Easy-Confocal optical system (spatial resolution < 1 μm) and two lasers (wavelengths of 785 nm and 532 nm). WiRE 3 software was used to acquire the data and images. In the experiments, green laser excitation was (532 nm) used for MnO$_2$ thin films, whereas red laser excitation (785 nm) was used for analysis of single MnO$_2$ nanowires supported on quartz.

QCM (Quartz Crystal Microbalance). The QCM measurements were performed with a Stanford Research Systems (SRS) QCM200 Quartz Crystal Microbalance Digital Controller, in conjunction with a QCM25 5 MHz Crystal Oscillator equipped with an Au-coated 5 MHz quartz crystal (area = 1.37 cm^2). The sensitivity factor (C_f) of the immersed quartz/gold electrode was calibrated by galvanostatically electrodepositing silver from aqueous 1 mM Ag$_2$SO$_4$, 0.1 M H$_2$SO$_4$. A second calibration, and a second C_f value appropriate for the emersed electrode, was obtained after drying the Ag film under vacuum for 2 h at room temperature. QCM analysis measures the frequency change, Δf, that is correlated with the mass loading, m, onto the quartz/Au electrode via the Sauerbrey equation:[38]

$$\Delta f = -C_f \Delta m \tag{9}$$

for the immersed gold QCM crystal, the value for C_f obtained from the silver calibration in the silver plating solution was 55.9 $\pm$0.7 Hz cm^2 μg^{-1}; for the dried silver deposit it was 49 $\pm$1 Hz cm^2 μg^{-1}.

XPS (X-ray Photoelectron Spectroscopy). XPS measurements were performed with an ESCALAB MKII (VG Scientific) surface analysis instrument. The ultrahigh vacuum multichamber system is equipped with a twin anode X-ray source (Mg/Al) and a 150 mm hemispherical electron energy analyzer. Spectra presented here were collected using Mg Kα X-rays (1253.6 eV) in constant energy mode with pass energy of 20 eV. During acquisition the base pressure of the spectroscopy chamber was 1 nTorr. Binding energies were calibrated using the C(1s) peak of adventitious carbon set at 284.8 eV as a reference.[39] Deconvolution and spectral line fitting were carried out using XPSPeak 4.1.

REFERENCES AND NOTES

1. Lee, H.; Manivannan, V.; Goodenough, J. Electrochemical Capacitors with KCl Electrolyte. *C. R. Acad. Sci. Ser. II Fasc. C—Chim.* **1999**, *2*, 565–577.
2. Wei, W.; Cui, X.; Chen, W.; Ivey, D. G. Manganese Oxide-Based Materials as Electrochemical Supercapacitor Electrodes. *Chem. Soc. Rev.* **2011**, *40*, 1697–1721.
3. Rolison, D. R.; Long, R. W.; Lytle, J. C.; Fischer, A. E.; Rhodes, C. P.; McEvoy, T. M.; Bourga, M. E.; Lubers, A. M. Multifunctional 3D Nanoarchitectures for Energy Storage and Conversion. *Chem. Soc. Rev.* **2009**, *38*, 226–252.
4. Long, J.; Dunn, B.; Rolison, D.; White, H. Three-Dimensional Battery Architectures. *Chem. Rev.* **2004**, *104*, 4463–4492.
5. Whittingham, M. Lithium Batteries and Cathode Materials. *Chem. Rev.* **2004**, *104*, 4271–4301.
6. Jiang, H.; Zhao, T.; Ma, J.; Yan, C.; Li, C. Ultrafine Manganese Dioxide Nanowire Network for High-Performance Supercapacitors. *Chem. Commun.* **2011**, *47*, 1264–1266.
7. Xia, H.; Feng, J.; Wang, H.; Lai, M. O.; Lu, L. MnO$_2$ Nanotube and Nanowire Arrays by Electrochemical Deposition for Supercapacitors. *J. Power Source* **2010**, *195*, 4410–4413.
8. Xu, C.; Zhao, Y.; Yang, G.; Li, F.; Li, H. Mesoporous Nanowire Array Architecture of Manganese Dioxide for Electrochemical Capacitor Applications. *Chem. Commun.* **2009**, 7575–7577.
9. Xiao, W.; Xia, H.; Fuh, J. Y. H.; Lu, L. Growth of Single-Crystal Alpha-MnO$_2$ Nanotubes Prepared by a Hydrothermal Route and Their Electrochemical Properties. *J. Power Source* **2009**, *193*, 935–938.
10. Chen, S.; Zhu, J.; Han, Q.; Zheng, Z.; Yang, Y.; Wang, X. Shape-Controlled Synthesis of One-Dimensional MnO$_2$ via a Facile Quick-Precipitation Procedure and its Electrochemical Properties. *Cryst. Growth Des.* **2009**, *9*, 4356–4361.
11. Liu, J.; Jiang, J.; Cheng, C.; Li, H.; Zhang, J.; Gong, H.; Fan, H. J. Co$_3$O$_4$ Nanowire@MnO$_2$ Ultrathin Nanosheet Core/Shell Arrays: A New Class of High-Performance Pseudocapacitive Materials. *Adv. Mater.* **2011**, *23*, 2076–2081.
12. Liu, J.; Essner, J.; Li, J. Hybrid Supercapacitor Based on Coaxially Coated Manganese Oxide on Vertically Aligned Carbon Nanofiber Arrays. *Chem. Mater.* **2010**, *22*, 5022–5030.
13. Liu, R.; Duay, J.; Lee, S. B. Redox Exchange Induced MnO$_2$ Nanoparticle Enrichment in Poly(3,4-ethylenedioxythiophene) Nanowires for Electrochemical Energy Storage. *ACS Nano* **2010**, *4*, 4299–4307.
14. Nam, H.-S.; Kwon, J. S.; Kim, K. M.; Ko, J. M.; Kim, J.-D. Supercapacitive Properties of a Nanowire-Structured

MnO$_2$ Electrode in the Gel Electrolyte Containing Silica. *Electrochim. Acta* **2010**, *55*, 7443–7446.

15. Fan, Q.; Whittingham, M. S. Electrospun Manganese Oxide Nanofibers as Anodes for Lithium-Ion Batteries. *Electrochem. Solid State Lett.* **2007**, *10*, A48–A51.

16. Toupin, M.; Brousse, T.; Bélanger, D. Charge Storage Mechanism of MnO$_2$ Electrode Used in Aqueous Electrochemical Capacitor. *Chem. Mater.* **2004**, *16*, 3184–3190.

17. Pang, S.; Anderson, M.; Chapman, T. Novel Electrode Materials for Thin-Film Ultracapacitors: Comparison of Electrochemical Properties of Sol-gel-Derived and Electrodeposited Manganese Dioxide. *J. Electrochem. Soc.* **2000**, *147*, 444–450.

18. Xiang, C.; Yang, Y.; Penner, R. M. Cheating the Diffraction Limit: Electrodeposited Nanowires Patterned by Photolithography. *Chem. Commun.* **2009**, 859–873.

19. Xiang, C.; Kung, S.-C.; Taggart, D. K.; Yang, F.; Thompson, M. A.; Gueell, A. G.; Yang, Y.; Penner, R. M. Lithographically Patterned Nanowire Electrodeposition: A Method for Patterning Electrically Continuous Metal Nanowires on Dielectrics. *ACS Nano* **2008**, *2*, 1939–1949.

20. Menke, E. J.; Thompson, M. A.; Xiang, C.; Yang, L. C.; Penner, R. M. Lithographically Patterned Nanowire Electrodeposition. *Nat. Mater.* **2006**, *5*, 914–919.

21. Nakayama, M.; Kanaya, T.; Lee, J.-W.; Popov, B. N. Electrochemical Synthesis of Birnessite-Type Layered Manganese Oxides for Rechargeable Lithium Batteries. *J. Power Source* **2008**, *179*, 361–366.

22. Bard, A. J.; Faulkner, L. R. *Electrochemical Methods: Fundamentals and Applications*, 2nd ed.; Wiley: New York, 2001.

23. Patterson, A. L. The Scherrer Formula for X-ray Particle Size Determination. *Phys. Rev.* **1939**, *56*, 978–982.

24. Hsu, Y.-K.; Chen, Y.-C.; Lin, Y.-G.; Chen, L.-C.; Chen, K.-H. Reversible Phase Transformation of MnO$_2$ Nanosheets in an Electrochemical Capacitor Investigated by *in Situ* Raman Spectroscopy. *Chem. Commun.* **2011**, *47*, 1252–1254.

25. Gao, T.; Fjellvag, H.; Norby, P. A Comparison Study on Raman Scattering Properties of Alpha- and Beta-MnO$_2$. *Anal. Chim. Acta* **2009**, *648*, 235–239.

26. Jana, S.; Pande, S.; Sinha, A. K.; Sarkar, S.; Pradhan, M.; Basu, M.; Saha, S.; Pal, T. A Green Chemistry Approach for the Synthesis of Flower-like Ag-Doped MnO$_2$ Nanostructures Probed by Surface-Enhanced Raman Spectroscopy. *J. Phys. Chem. C* **2009**, *113*, 1386–1392.

27. Julien, C.; Massot, M.; Baddour-Hadjean, R.; Franger, S.; Bach, S.; Pereira-Ramos, J. Raman Spectra of Birnessite Manganese Dioxides. *Solid State Ionics* **2003**, *159*, 345–356.

28. Chigane, M.; Ishikawa, M. Manganese Oxide Thin Film Preparation by Potentiostatic Electrolyses and Electrochromism. *J. Electrochem. Soc.* **2000**, *147*, 2246–2251.

29. Toupin, M.; Brousse, T.; Bélanger, D. Influence of Microstucture on the Charge Storage Properties of Chemically Synthesized Manganese Dioxide. *Chem. Mater.* **2002**, *14*, 3946–3952.

30. Luo, J.; Suib, S. Preparative Parameters, Magnesium Effects, and Anion Effects in the Crystallization of Birnessites. *J. Phys. Chem. B* **1997**, *101*, 10403–10413.

31. Villalobos, M.; Lanson, B.; Manceau, A.; Toner, B.; Sposito, G. Structural Model for the Biogenic Mn Oxide Produced by *Pseudomonas putida*. *Am. Mineral.* **2006**, *91*, 489–502.

32. Post, J.; Veblen, D. Crystal-Structure Determination of Synthetic Sodium, Magnesium, and Potassium Birnessite Using TEM and the Rietveld Method. *Am. Miner.* **1990**, *75*, 477–489.

33. Brezesinski, T.; Wang, J.; Polleux, J.; Dunn, B.; Tolbert, S. H. Templated Nanocrystal-Based Porous TiO$_2$ Films for Next-Generation Electrochemical Capacitors. *J. Am. Chem. Soc.* **2009**, *131*, 1802–1809.

34. Lindstrom, H.; Sodergren, S.; Solbrand, A.; Rensmo, H.; Hjelm, J.; Hagfeldt, A.; Lindquist, S. Li$^+$ Ion Insertion in TiO$_2$ (anatase). 2. Voltammetry on Nanoporous Films. *J. Phys. Chem. B* **1997**, *101*, 7717–7722.

35. Liu, T.; Pell, W.; Conway, B.; Roberson, S. Behavior of Molybdenum Nitrides as Materials for Electrochemical

36. Brezesinski, K.; Wang, J.; Haetge, J.; Reitz, C.; Steinmueller, S. O.; Tolbert, S. H.; Smarsly, B. M.; Dunn, B.; Brezesinski, T. Pseudocapacitive Contributions to Charge Storage in Highly Ordered Mesoporous Group V Transition Metal Oxides with Iso-oriented Layered Nanocrystalline Domains. *J. Am. Chem. Soc.* **2010**, *132*, 6982–6990.

37. Wang, J.; Polleux, J.; Lim, J.; Dunn, B. Pseudocapacitive Contributions to Electrochemical Energy Storage in TiO$_2$ (Anatase) Nanoparticles. *J. Phys. Chem. C* **2007**, *111*, 14925–14931.

38. Sauerbrey, G. Verwendung von Schwingquarzen zur Wägung dünner Schichten und zur Mikrowägung (Use of Quartz Oscillators for Weighing Thin Layers and for Microweighing). *Z. Phys.* **1959**, *155*, 206–222.

39. Wagner, C. D.; Naumkin, A. V.; Kraut-Vass, A.; Allison, J. W.; Rumble, J. R., Jr. *NIST X-ray Photoelectron Spectroscopy Database* http://srdata.nist.gov/XPS.

40. Hosono, E.; Kudo, T.; Honma, I.; Matsuda, H.; Zhou, H. Synthesis of Single Crystalline Spinel LiMn$_2$O$_4$ Nanowires for a Lithium Ion Battery with High Power Density. *Nano Lett.* **2009**, *9*, 1045–1051.

41. Nam, K.-W.; Lee, C.-W.; Yang, X.-Q.; Cho, B. W.; Yoon, W.-S.; Kim, K.-B. Electrodeposited Manganese Oxides on Three-Dimensional Carbon Nanotube Substrate: Supercapacitive Behaviour in Aqueous and Organic Electrolytes. *J. Power Source* **2009**, *188*, 323–331.

42. Zou, W.-y.; Wang, W.; He, B.-l.; Sun, M.-l.; Yin, Y.-s. Supercapacitive Properties of Hybrid Films of Manganese Dioxide and Polyaniline Based on Active Carbon in Organic Electrolyte. *J. Power Source* **2010**, *195*, 7489–7493.

43. Ma, S.-B.; Nam, K.-W.; Yoon, W.-S.; Yang, X.-Q.; Ahn, K.-Y.; Oh, K.-H.; Kim, K.-B. Electrochemical Properties of Manganese Oxide Coated onto Carbon Nanotubes for Energy-Storage Applications. *J. Power Source* **2008**, *178*, 483–489.

44. Kim, J.-H.; Lee, K. H.; Overzet, L. J.; Lee, G. S. Synthesis and Electrochemical Properties of Spin-Capable Carbon Nanotube Sheet/MnO$_x$ Composites for High-Performance Energy Storage Devices. *Nano Lett.* **2011**, *11*, 2611–2617.

45. Chin, S.; Pang, S.; Anderson, M. Material and Electrochemical Characterization of Tetrapropylammonium Manganese Oxide Thin Films as Novel Electrode Materials for Electrochemical Capacitors. *J. Electrochem. Soc.* **2002**, *149*, A379–A384.

46. Lang, X.; Hirata, A.; Fujita, T.; Chen, M. Nanoporous Metal/Oxide Hybrid Electrodes for Electrochemical Supercapacitors. *Nat. Nanotechnol.* **2011**, *6*, 232–236.

47. Broughton, J.; Brett, M. Investigation of Thin Sputtered Mn Films for Electrochemical Capacitors. *Electrochim. Acta* **2004**, *49*, 4439–4446.

48. Carver, J.; Carlson, T.; Schweitz, G. Use of X-ray Photoelectron Spectrscopy to Study Bonding in Cr, Mn, Fe, and Co Compounds. *J. Chem. Phys.* **1972**, *57*, 973–&.

49. Oku, M.; Hirokawa, K.; Ikeda, S. X-ray Photoelectron-Spectroscopy of Manganese—Oxygen Systems. *J. Electron Spectrosc. Relat. Phenom.* **1975**, *7*, 465–473.

50. Aoki, A. X-ray Photoelectron Spectroscopic Studies on ZnS-MnF$_2$ Phosphors. *Jpn. J. Appl. Phys.* **1976**, *15*, 305–311.

51. Oku, M.; Hirokawa, K. X-ray Photoelectron-Spectroscopy of Co$_3$O$_4$, Fe$_3$O$_4$, Mn$_3$O$_4$, and Related Compounds. *J. Electron Spectrosc. Relat. Phenom.* **1976**, *8*, 475–481.

52. Ivanovemin, B.; Nevskaya, N.; Zaitsev, B.; Ivanova, T. Synthesis and Properties of Calcium and Strontium Hydromanganates-(III). *Zh. Neorgan. Khim.* **1982**, *27*, 3101–3104.

53. Strohmeier, B.; Hercules, D. Surface Spectroscopic Characterization of Mn/Al$_2$O$_3$ Catalysts. *J. Phys. Chem.* **1984**, *88*, 4922–4929.

54. Dicastro, V.; Polonetti, G. XPS Study of MnO Oxidation. *J. Electr. Spectrosc. Rel. Phen.* **1989**, *48*, 117–123.

55. Tan, B.; Klabunde, K.; Sherwood, P. XPS Studies of Solvated Metal Atom Dispersed Catalysts—Evidence for Layered Cobalt Manganese Particles on Alumina and Silica. *J. Am. Chem. Soc.* **1991**, *113*, 855–861.

56. Allen, G.; Harris, S.; Jutson, J.; Dyke, J. A Study of a Number of Mixed Transition-Metal Oxide Spinels Using X-ray

Photoelectron Spectroscopy. *Appl. Surf. Sci.* **1989**, *37*, 111–134.

57. Nefedov, V.; Gati, D.; Dzhurinskii, B.; Sergushin, N.; Salyn, Y. X-Ray Electron Study of Oxides of Elements. *Zh. Neorgan. Khim.* **1975**, *20*, 2307–2314.

58. Umezawa, Y.; Reilley, C. Effect of Argon Ion-Bombardment of Metal-Complexes and Oxides Studied by X-Ray Photo-electron Spectroscopy. *Anal. Chem.* **1978**, *50*, 1290–1295.